

# SPATIAL METRICS THAT FACILITATE THE COMPARISON OF RADAR REFLECTIVITY VALUES WITHIN LANDFALLING TROPICAL CYCLONES

14B.6

Corene J. Matyas<sup>1</sup> \*, Stephanie Zick<sup>2</sup>, Jingyin Tang<sup>3</sup>

<sup>1</sup>University of Florida, Gainesville, Florida; <sup>2</sup>Virginia Tech, Blacksburg, VA, <sup>3</sup>The Weather Company/ IBM, Atlanta, GA

## 1. INTRODUCTION

Tropical cyclones (TCs) undergo structural changes that have important implications for the damage they cause when over land. Numerical weather prediction (NWP) models, such as the Weather Research and Forecasting (WRF) model, have been used to examine TC interactions with the surrounding environment (Davis et al. 2008; Hill and Lackmann 2009; Au-Yeung and Chan 2010; Kellner et al. 2012; Li et al. 2014). However, most studies base their comparisons of spatial features on visual inspection rather than on measures of the shapes of these features.

Measuring the spatial attributes of precipitating regions within TCs permits the quantification of changes in size, shape, and location of precipitation regions. For example, the Dvorak technique diagnoses TC intensity using the spatial arrangement of its cloud features (Dvorak 1975; Velden et al. 2006). With observations from ground-based radar, fine-scale shapes can be measured to examine storm structure during landfall. For example, Matyas (2007, 2008; Matyas 2010b) utilized reflectivity data from the Weather Surveillance Radar 1988 Doppler (WSR-88D) network to demonstrate that 20 dBZ rain regions become more elongated and fragmented after landfall (Matyas 2007, 2008) and 40 dBZ regions spread outward from the storm center as TCs weaken after landfall (Matyas (2010a).

In this study, we examine a landfalling hurricane to demonstrate 1) the degree to which five spatial metrics quantify changes in storm structure, 2) that these metrics facilitate comparisons among observations and simulations of a TC, and 3) that these metrics can be utilized across datasets of differing spatial and temporal resolutions. Observations of radar reflectivity from the WSR-88D network

\* Corresponding author address:

Corene J. Matyas, Univ. of Florida, Dept. of Geography, Gainesville, FL 32611-7315; e-mail matyas@ufl.edu

are compared to simulated reflectivity in WRF model simulations while the TC moves over land. The radar observations are also compared with those from the Tropical Rainfall Measuring Mission (TRMM) 3B42 dataset to match reflectivity values to rain rates, and the shapes of these rain rate regions are examined during the hurricane's entire lifecycle.

## 2. DATA AND METHODS

We investigate the spatial evolution of reflectivity regions during the landfall and extratropical transition (ET) of Hurricane Isabel (2003). Operational forecast models had good predictions of track and extent of rainfall (NOAA 2003), and thus, we expect that a research-grade simulation should perform well. Isabel made landfall at 1700 UTC 18 September 2003 (Lawrence et al. 2005), and WSR-88D data are available while the storm was over land. Isabel was declared post-tropical at 1200 UTC 19 September while its center was over the U.S., providing an opportunity to measure changes in structure during the ET process. As such, the spatial metrics we explore focus on representation of synoptic-to mesoscale processes.

We process Level II reflectivity data (NOAA 1991) from WSR-88D stations within 600 km of the storm center. We use spline interpolation to obtain 30-minute positions for the storm center from the 6-hourly best track (BT) data. After quality control and pre-processing, data are gridded at 3 km x 3 km x 0.5 km resolution using a 10-minute moving window. Values for grid cells with data from multiple radars retain the highest reflectivity value. Cells with missing values are filled using a distance-weighted interpolation. Additionally, we compare reflectivity values across a constant altitude of 3.5 km above mean sea level, which is more than one kilometer below the melting level.

Analysis begins at 1800 UTC 18 September as this is the first hour that all rainbands are inside of the region detectable by the radar network. Analysis concludes at 0900



Metric	Equation	Near 0	Near 1
Circularity	$Cl = \frac{\text{Length minor axis}}{\text{Length major axis}}$		
Solidity	$S = \frac{\text{Area}}{\text{Convex Area}}$		
Closure	$Cl = \frac{\text{no. } 1^\circ \text{ angles intersecting polygons}}{360}$		
Dispersion	$D = \frac{\sum_{i=1}^{NP} Area_i (r_{centroid_i})}{\sum_{i=1}^{NP} Area_i (r_{search})}$		
Fragmentation	$F = 1 - \left( \frac{\sum_{i=1}^{NP} Area_i}{ConvexArea} \right) \left( 1 - \frac{NP - 1}{NP + \sqrt{\#pixels}} \right)$		

Fig. 3 Five spatial metrics, their equations, and examples of low and high-end shapes.

Reflectivity values of 20 dBZ represent light rainfall. Many researchers have used this threshold to define the edge of a TC (e.g., Jorgensen 1984; Matyas 2007; Hazelton and Hart 2013). Thus, we measure the shape of the largest polygon representing regions of 20 dBZ or greater. *Circularity* (Stoddart 1965) is computed by enclosing the largest polygon within a rectangle and measuring its width and length. To calculate *solidity* (Jiao et al. 2012), we construct a polygon representing the convex hull around the rainfall region that represents the smallest yet simplest polygon that can enclose another polygon. Solidity compares the area of the reflectivity region to the area of the convex hull.

As in previous research (Jorgensen 1984; Steiner et al. 1995; Skwira et al. 2005; Matyas 2009; Matyas 2010a), we select 40 dBZ to represent higher rain rates associated with convective precipitation. For polygons bounded by 20 and 40 dBZ reflectivity values, we calculate three metrics to characterize the entire rain field utilizing a search radius that extends 600 km from the storm center. We define the center using minimum sea level pressure (for WRF simulations) and interpolated 30 minute positions (for WSR-88D) from HURDAT.

Similar to the rain shield arc length calculated in Matyas (2007), *closure* measures the distribution of reflectivity in the azimuthal direction. We only consider radial distances 50-600 km from the storm center to buffer for TC

position errors due to the vertical tilt of the vortex, and/or interpolation of the storm center. The presence of reflectivity is evaluated at each 1° angle and the number of intersections is divided by 360 to obtain a value in the 0-1 range.

*Dispersion* (Massam and Goodchild 1971) measures the radial distribution of precipitation, with small values indicating that the mass of precipitation is close to the center. Dispersion increases to a value of one as the reflectivity region centroid(s) ( $r_{centroid}$ ) move radially away from the circulation center and have their centroids located at the edge of the search radius ( $r_{search}$ ). Each reflectivity region is weighted by its area, and the final metric is calculated by summing over all reflectivity regions, with NP representing the number of polygons.

*Fragmentation* (AghaKouchak et al. 2011) is an inverse measure of the product of the solidity and connectivity of the precipitation pattern. This metric increases as individual objects split into multiple regions, which decreases connectivity. If those objects gain more holes, this decreases solidity.

### 3. RESULTS

#### 3.1 WSR reflectivity and relationships with synoptic-scale conditions

First, we calculate Spearman's rank correlation coefficients to measure the strength and direction of association among the WSR reflectivity levels (Table 1). These results justify our selection of 20 and 40 dBZ for comparison with simulated reflectivity, with 20 and 25 dBZ being strongly correlated, and 35 and 40 dBZ being strongly correlated. Closure has a larger difference among the reflectivity levels (Fig. 4a) than dispersion (Fig. 4b) and fragmentation (Fig. 4c). While 20-30 dBZ started with complete closure and values never fell below 0.6, 35 and 40 dBZ values indicate exposure at the outset that increases. Closure for 40 dBZ is highly correlated with 35 dBZ but less so with lower reflectivity values. Dispersion depicts a slow increase over time (Fig. 4b). Values for 20-30 dBZ are strongly correlated. However, 40 and 20 dBZ values are not significantly correlated, and the correlation between 20 and 35 dBZ is weak. When examining fragmentation, 20 and 25 dBZ have an increasing trend and are strongly correlated, while 35 and 40 dBZ display little

change and are strongly correlated (Fig. 4c). Collectively, these results indicate that spatial organization differs between regions of lower rain rates represented by 20 and 25 dBZ values, comprised of stratiform precipitation, and those of higher rain rates from convective precipitation represented by 35 and 40 dBZ values.

Table 1. Spearman’s rank correlation coefficients for spatial metrics across differing WSR reflectivity levels and time.

Reflectivity Level (dBZ)	25	30	35	40	Time
Closure 20	<b>0.95</b>	<b>0.86</b>	<b>0.59</b>	0.36	-0.52
Closure 25		<b>0.87</b>	<b>0.62</b>	0.40	-0.55
Closure 30			<b>0.79</b>	<b>0.55</b>	-0.71
Closure 35				<b>0.84</b>	-0.92
Closure 40					-0.91
Disp 20	<b>0.89</b>	<b>0.67</b>	0.38	0.30	0.68
Disp 25		<b>0.82</b>	<b>0.63</b>	<b>0.60</b>	0.82
Disp 30			<b>0.79</b>	<b>0.67</b>	0.89
Disp 35				<b>0.83</b>	0.71
Disp 40					0.70
Frag 20	<b>0.83</b>	0.19	-0.11	-0.27	0.85
Frag 25		0.25	-0.16	-0.38	0.83
Frag 30			-0.09	0.01	<b>0.53</b>
Frag 35				<b>0.41</b>	-0.08
Frag 40					-0.32

**Significant at  $\alpha = 0.01$**

All metrics save for 35 and 40 dBZ fragmentation exhibit a strong correlation with time (Table 1). Thus, rainfall regions generally spread outwards from the storm center, the center becomes more exposed, and regions of lighter rainfall become more fragmented. Although strong synoptic-scale forcing is likely the dominant mechanism responsible for these changes, interaction with topography may also contribute to changes in storm structure. Had orographic enhancement played the primary role in generating precipitation, dispersion would have decreased as the circulation center moved closer to the stationary location of precipitation enhancement. However, topographic forcing may be responsible for increases in closure for the 20 and 25 dBZ reflectivity values 0300-0700 UTC (Fig. 4a). During this period, smaller regions of rainfall developed over elevated terrain (Fig. 5, small regions located near blue and purple arrows and buffer outline) as Isabel’s center crossed the Appalachian Mountains.

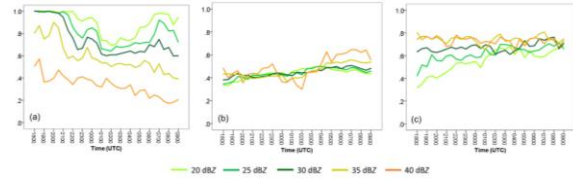


Fig. 4 Time series of metric values for five reflectivity thresholds a) closure, b) dispersion, c) fragmentation.

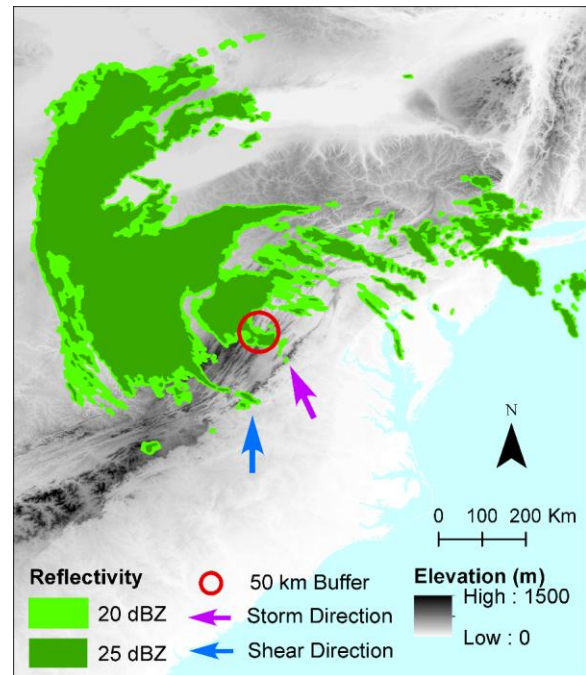


Fig. 5 Reflectivity regions with vectors of motion and vertical wind shear as Isabel moves over the Appalachian Mountains.

When a TC undergoes ET, vertical wind shear and storm velocity increase as the TC interacts with the middle latitude westerlies while relatively dry air is entrained into the storm’s core (Harr and Elsberry 2000; Klein et al. 2000; Hart and Evans 2001; Jones et al. 2003). To associate these conditions with changes in the spatial metrics, we utilize a Geographic Information System to calculate values from the NCEP Global Forecasting System (GFS) model final analyses. Deep-layer vertical wind shear is calculated by subtracting values at 850 hPa from those at 200 hPa and averaging over an annular region 200-800 km from center. The shear vector has a southwesterly or southerly direction. Precipitation tends to be enhanced downshear (Rogers et al. 2003; Chen et al. 2006; Cecil 2007), and this pattern occurred in our case study as the centroids of the 20 dBZ

reflectivity regions were located  $35^{\circ}$ - $55^{\circ}$  left of shear. Storm velocity increased during the ET period. Rainfall tends to be enhanced in the right front and downshear left quadrants, and these quadrants tend to overlap for Atlantic basin TCs (Corbosiero and Molinari 2003; Chen et al. 2006; Matyas 2010b). In Isabel's case, the motion vector is only  $30$ - $40^{\circ}$  left of the shear vector. The centroids of the largest 20 dBZ reflectivity regions shifted from  $5^{\circ}$  right to  $20^{\circ}$  left of the storm motion vector.

When Isabel moves poleward, decreasing moisture should erode the rain field. Thus, closure should decrease and dispersion and fragmentation should increase as drier air enters the storm's core. As expected, TPW generally decreases 24 hours prior to landfall. Matyas (2017) showed that TC rainfall is greater when TPW values of 45 mm extend from the deep tropics into the TC's circulation. The moisture distribution around Isabel fits this pattern, with 45 mm of TPW extending southward into the deep tropics throughout the study period. The entire region south of the circulation center contains values  $\geq 45$  mm at 0000 UTC 18 Sep (Fig. 6a). Eighteen hours later, values of 35 and 25 mm surround the southwest quadrant of the storm (Fig. 6b). Six and 12 hours later, these TPW values migrate counterclockwise south and southeast of center, respectively (Figs. 6c, d). The reduction of TPW near the storm's inner core coincides with the erosion of rainfall there and increasing dispersion and fragmentation. Additionally, the increase in dry air around the TC coincides with decreasing closure values (Fig. 4a). Throughout the period, the outermost rainband is positioned near the western edge of the 45 mm TPW contour.

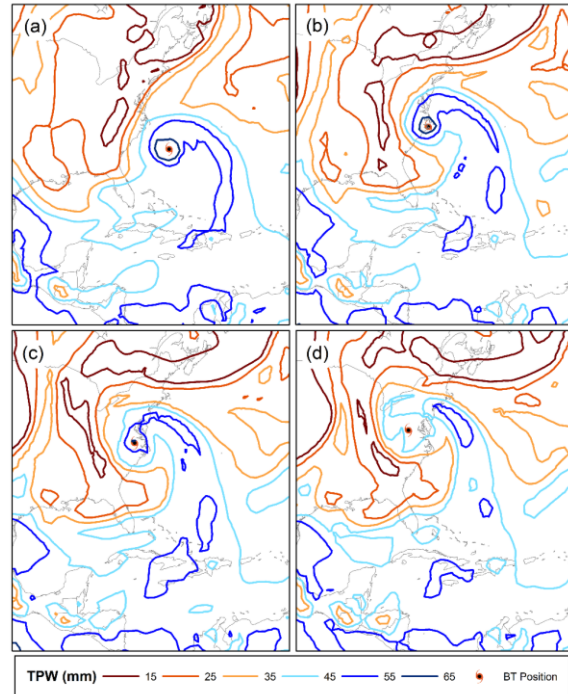


Fig. 6 Spatial pattern of total precipitable water (TPW) at (a) 0000 UTC 18 September, (b) 1800 UTC 18 September, (c) 0000 UTC 19 September, and (d) 0600 UTC 19 September.

### 3.2 WRF model setup

We now compare the observed reflectivity regions with those produced through simulations utilizing version 3.6.1 of the Advanced Research Weather Research and Forecasting (WRF-ARW) model (Wang et al. 2012). Please consult Matyas et al. (2018) for a full discussion of the WRF set-up. The innermost of the triple nest has a 3 km grid length and we place the data on the same grid as the WSR-88D values. We perform our analysis on the model-simulated reflectivity factor.

To vary the spatial configurations of the TC rainbands so that we can demonstrate the utility of the spatial metric approach, we create a set of simulations by varying the cumulus and microphysics parameterizations. For the cumulus parameterization, we employ the modified Tiedtke (Tiedtke 1989) and Kain-Fritsch (Kain and Fritsch 1990; Kain 2004) schemes. The Tiedtke scheme is recommended for hurricane simulations in the WRF 3.6.1 documentation and the Kain-Fritsch scheme has been employed in a WRF simulation of Hurricane Isabel (2003) (Lin et al. 2010), and the

hurricane nature run (Nolan et al. 2013). The set of six simulations employs three microphysics schemes. Each has six mass variables (water vapor, cloud droplets, cloud ice, rain, snow, and graupel) but increase in complexity with number concentration variables and their representation of cloud physical processes. The WRF 6-class single moment (WSM6) scheme (Hong et al. 2006) is used operationally and in numerous TC research studies. The WRF 6-class double moment (WDM6) scheme (Lim and Hong 2010) predicts number concentrations for cloud, rainwater, and cloud condensation nuclei, thus it is a partially double moment scheme. Nolan et al. (2013) employ WDM6 for the hurricane nature run. We select Morrison-2M (Morrison et al. 2009) for a scheme that is fully double-moment. It predicts the mixing ratios and number concentrations of cloud droplets, cloud ice, snow, rain, and graupel. As each cumulus parameterization is paired with each of the microphysics schemes, our six simulations are: Tiedtke WSM6 (TS), Tiedtke WDM6 (TD), Tiedtke Morrison (TM), Kain-Fritsch WSM6 (KFS), Kain-Fritsch WDM6 (KFD) and Kain-Fritsch Morrison (KFM). We also calculate bias in the simulated and observed reflectivity values utilizing their areal coverage, and apply a correction factor prior to calculating the spatial metrics. Details of this analysis are available in Matyas et al. (2018).

### 3.3 Spatial metric results for 20 dBZ polygons

Among the metrics, circularity of the largest polygon shows the greatest contrast between the Kain-Fritsch and Tiedtke simulations (Fig. 7a). The Kain-Fritsch simulations feature circular shapes due to the lack of a separate outer rainband. The arc of the main polygon in the KFS simulation encircles the storm center and has the most circular shape during the first six hours, while KFM is more elongated until rainfall develops in an arc to the north of the center around 2300 UTC (Fig. 8a, b). The Tiedtke simulations have an elongated outer rainband that separates from the inner core region (Fig. 8c, d). However, at 0200 UTC, erosion of the outer rainband means that the circular-shaped inner core becomes the main polygon in the TS simulation. In TM, this occurs at 0300 UTC. For WSR, erosion of rainfall southeast of the storm center while the outer rainband expands northward causes circularity to decrease around

2000 UTC and remain low until 0300 UTC. Over the next three hours, rainfall develops eastward (Fig. 9), extending the minor axis and leading to a more circular shape.

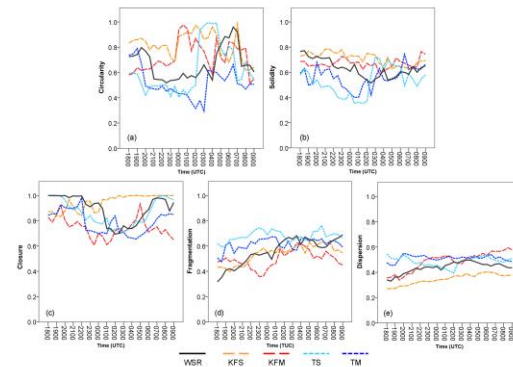


Fig. 7 Time series of (a) circularity, and (b) solidity (for the largest 20 dBZ polygon) and (c) closure, (d) fragmentation, and (e) dispersion metrics (for all 20 dBZ polygons).

Having higher solidity means that more of the main polygon's convex hull is filled with reflectivity values. The WSR polygon exhibits the highest solidity at 1800 UTC, but values decrease (Fig. 7b) due to rainfall eroding 1) from southeast to northeast and 2) between the outer rainband and inner core (Fig. 9). Erosion of the southern portion of the outer rainband allows the convex hull to grow smaller after 0300 UTC. The Kain-Fritsch solidity values remain consistent while Tiedtke values are lower (Fig. 7b). The more elongated outer rainband in the Tiedtke simulations produces a convex hull that is much larger than the Kain-Fritsch simulations' more compressed main rainfall region.

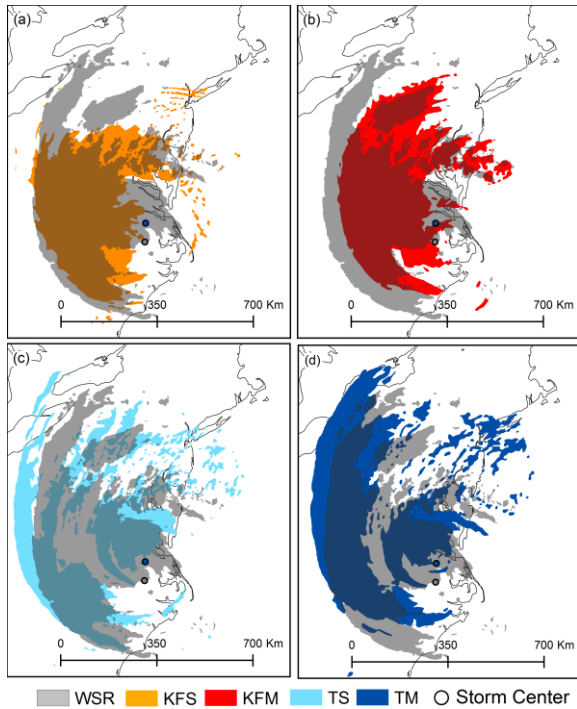


Fig. 8 Polygons representing reflectivity values of 20 dBZ or higher at 2230 UTC 18 September for WSR (gray) and (a) KFS, (b) KFM, (c) TS, and (d) TM.

The closure metric (Fig. 7c) represents how much of the 360° arc around the TC center is occupied by reflectivity. The median value for WSR is 0.88 (317°). The TS simulation is most similar to WSR as both centers remain encircled by 20 dBZ values for the first three hours (Fig. 8c). The rate of opening for WSR over the next 6.5 hours approximates 16.5° per hour. Redevelopment of rainfall south and eventually east of center allows the TS simulation to depict complete closure by 0700 UTC, while rainfall is not present in these areas for WSR. Although the Morrison-2m simulations feature lower values due to less rainfall east of center, closure generally decreases from 2000 to 0000 UTC. The least successful simulation for this metric is KFS. Beginning at 0000 UTC, a rainband connected to the storm's inner core grows from the east to the south, maximizing closure.

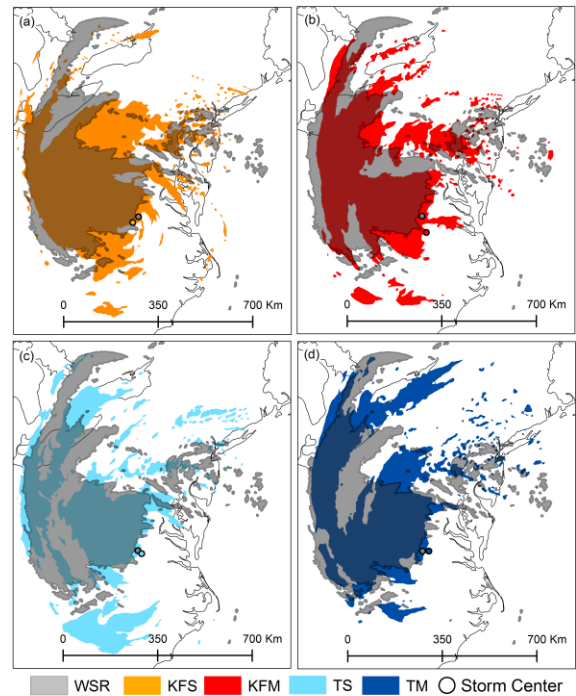


Fig. 9 As in Fig. 8 but at 0400 UTC 19 September.

The highest range of fragmentation occurs in WSR (Fig. 7d). The Kain-Fritsch simulations are less fragmented compared to the Tiedtke simulations, where many small polygons exist north and northwest of the center (Fig. 8). The greatest disagreement among the four simulations occurs early in the period, with better agreement achieved 0200-0500 UTC when fragments are observed north and northeast of center (Fig. 9).

As landfall and ET progress, we expect dispersion to increase. This trend is evident in WSR, with an increase of 0.015 per hour until 0400 UTC (Fig. 7e). Although the ranges of dispersion values differ among the simulations, the KFS values are much lower due to the storm's compressed shape. The Tiedtke simulations are the most fragmented and the consistently high dispersion values mean that these polygons are located farther from the circulation center.

#### 4. COMPARING WSR AND TRMM 3B42

The TRMM 3B42 product (Huffman et al. 2007) blends observations from satellites to produce a snapshot of rain rates every three hours on a grid at a resolution of 0.25° latitude

and longitude. Although employed by numerous TC researchers (e.g., Shepherd et al. 2007; Jiang et al. 2011; Matyas 2014), these data are relatively coarse when compared with WSR observations. However, they allow TC rain fields to be monitored before, during, and after landfall (Fig. 10). Thus, we evaluate four metrics that measure the shape of rain fields across these datasets with different spatial resolutions.

First, we utilize the area covered to find the best match between reflectivity regions and rain rate regions. We analyze the TRMM data by contouring rain rate values every 1 mm/hr and comparing the metrics during seven observation times where WSR and TRMM data overlap. The following rain rates in TRMM were acceptable matches for the reflectivity levels: 2 mm/hr and 20 dBZ, 3 mm/hr and 25 dBZ, 5 mm/hr and 30 dBZ. Once reflectivity values reached 35 dBZ, the TRMM areas were not well-matched with 7 mm/hr being too low and 8 mm/hr matching at first but ending too high as landfall progressed. These results agree with previous research (Zagrodnik and Jiang 2013; Zhou and Matyas 2018a) that defined 2.5 mm/hr as a threshold for light rainfall, and 5 mm/hr as a threshold for moderate rainfall.

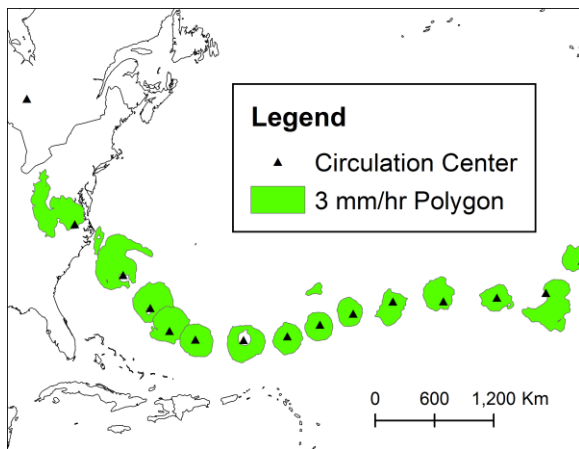


Fig. 10 Center of Isabel's circulation and rain fields using the 3 mm/hr threshold every 24 hours beginning at 0000 UTC September 6, 2003.

When comparing the spatial metric values for the matched radar reflectivity and TRMM rain rates, results were inconsistent. The closest match was with dispersion, with lower rain rates only slightly higher for TRMM than radar (Fig. 11a). For fragmentation, all values were higher for radar (Fig. 11b), likely due to their higher resolution so that more fragments were

detected. In most instances, only one polygon was present in the TRMM analysis. For lower values, circularity was higher in the radar data but the opposite occurred for higher values (Fig. 11c). Regions of higher rainfall in the outer rain bands tend to more elongated (Matyas 2009) and were the largest polygon for the radar analysis, while they were more circular due to the resolution of the TRMM data. The lower solidity of radar polygons (Fig. 11d) was due to erosion of rainfall between the inner core and outer region rainbands that was not detected in the more coarse TRMM data. We did not analyze closure due to mismatches between the TRMM values and interpolated circulation center positions (Fig. 10).

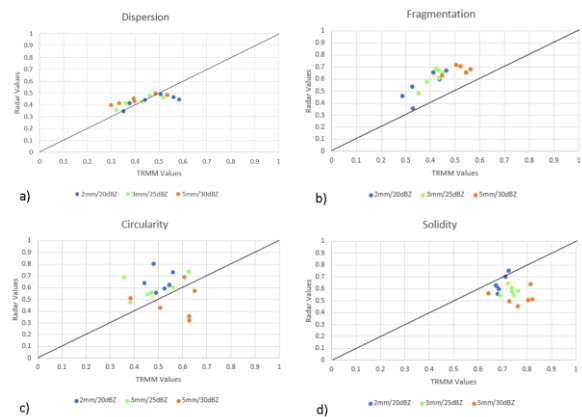


Fig. 11 Comparison of spatial metric values for paired radar reflectivity and TRMM rain rate values.

We then examine the four metrics over Isabel's lifecycle (Fig. 12). Although all metrics were strongly correlated to one another, dispersion produced the most agreement among the three rain rates and exhibited the smoothest trends (Fig. 12a). Given the large search radius, rainfall must shift several kilometers radially to affect the value. We then correlated metric values with data pertaining to storm motion and intensity from HURDAT, and vertical wind shear and moisture obtained from the Statistical Hurricane Intensity Prediction Scheme database (DeMaria et al. 2005). Changes in dispersion coincided well with changes in storm intensity, which was expected as the spatial arrangement of clouds is used to determine storm intensity (Dvorak 1975). Dispersion decreased greatly when rain fields became more compact as Isabel intensified from a minor to major hurricane, and values remained low for seven

days while intensity fluctuated between Categories 4 and 5. Expansion began around 0600 UTC on September 15 and continued through landfall.

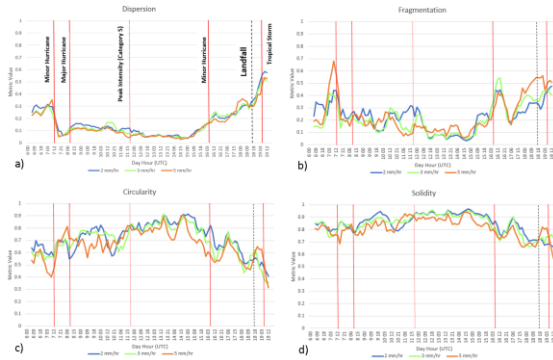


Fig. 12 Spatial metric values for the three rain rate thresholds for: a) dispersion, b) fragmentation, c) circularity, d) solidity. The red lines indicate important changes in storm intensity as indicated in a), and the black dashed line indicates the time of landfall.

Relative humidity in the lower troposphere remained high during Isabel’s lifecycle and was not strongly correlated with rain field organization (Table 2). However, higher levels of moisture in the middle and upper troposphere were more strongly correlated with higher fragmentation and dispersion, and lower solidity and circularity. These results indicate that when more moisture was available over a deeper layer of the troposphere, rainfall developed farther from the circulation center, which agrees with Zhou and Matyas (2018b) who utilized TRMM data to examine TCs moving over the Caribbean Sea and Gulf of Mexico. Correlations between shear and the shape metrics were fairly weak.

Table 2 Spearman’s rank correlation coefficients averaged across the three rain rate thresholds for each condition and spatial metric. Bold values are statistically significant at 0.01.

<i>Condition</i>	<i>Disp</i>	<i>Frag</i>	<i>Circular</i>	<i>Solid</i>
Max Wind Speed	<b>-0.83</b>	<b>-0.70</b>	<b>0.81</b>	<b>0.79</b>
Storm Motion Speed	0.20	0.13	-0.23	<b>-0.26</b>
Deep-Layer Shear	<b>0.26</b>	<b>0.26</b>	-0.17	<b>-0.31</b>
Shallow Shear	<b>0.26</b>	0.12	-0.18	-0.17
Low-Tropo Moisture	0.23	0.23	<b>-0.30</b>	<b>-0.27</b>
Mid-Tropo Moisture	<b>0.39</b>	<b>0.40</b>	<b>-0.41</b>	<b>-0.48</b>
High-Tropo Moisture	<b>0.39</b>	<b>0.42</b>	<b>-0.37</b>	<b>-0.48</b>

## 5. CONCLUSIONS

This study employed spatial metrics to compare reflectivity values observed by ground-based radars, produced by simulations, and rain rates detected by satellites. Hurricane Isabel (2003) was utilized as a case study. The spatial metrics quantified changes in rainband structure as observed by the WSR-88D network as Isabel encountered relatively dry air and strong vertical wind shear while moving inland. Rainfall became less solid and more fragmented as it spread outward from and enclosed less of the storm center. For low reflectivity regions, changes in dispersion and fragmentation occurred linearly while solidity and closure decreased at first and later increased. By delineating and measuring the shape and location of light and heavy rainfall regions, we provide a quantification for spatial changes that agrees with qualitative descriptions of TC structural changes after landfall and during ET (Klein et al. 2000; Atallah et al. 2007; Villarini et al. 2011) and advances the work of Matyas (2007, 2008; 2010a) and Zick and Matyas (2016).

The correlation analyses revealed that metrics exhibit a more similar trend over time when simulations feature the same cumulus scheme than when they utilize the same microphysics scheme. At landfall, the Tiedtke simulations produced a rain field that was more fragmented and dispersed from the storm center and, at most times, lacked a connecting band between the inner core and outer rainband. The Tiedtke simulations also featured larger regions of high reflectivity near the storm center, and dispersion increased rapidly as these regions eroded. In contrast, the Kain-Fritsch simulations produced a more compressed, solid, and circular region of reflectivity whose area did not erode as quickly.

Although we only simulated one TC and findings may not be representative for all TCs, our results suggest that future studies should employ similar methods for 1) comparing the evolving spatial patterns in TC rainfall regions among simulations and to observed values, and 2) comparing rainband configurations produced by different operational forecast models or observed by more coarse-resolution satellites. Landfalling TCs that are not affected by trough interaction should be examined to 1) determine if erosion of rainfall on the outer edges of the storm leads to increased rates of fragmentation without increased dispersion and 2) if the storm center becomes exposed at a different rate

compared with storms undergoing ET. Also, additional metrics should be calculated to examine the orientation and displacement of the reflectivity regions relation to shear and motion vectors.

## 6. ACKNOWLEDGEMENTS

This research was funded the National Science Foundation BCS-1053864. Gary Lackmann provided feedback on this project.

## 7. REFERENCES

- AghaKouchak, A., N. Nasrollahi, J. Li, B. Imam, and S. Sorooshian, 2011: Geometrical characterization of precipitation patterns. *J. Hydrometeorol.*, **12**, 274-285.
- Atallah, E. H., L. F. Bosart, and A. R. Aiyyer, 2007: Precipitation distribution associated with landfalling tropical cyclones over the eastern United States. *Mon. Wea. Rev.*, **135**, 2185-2206.
- Au-Yeung, A. Y. M., and J. C. L. Chan, 2010: The effect of a river delta and coastal roughness variation on a landfalling tropical cyclone. *J. Geophys. Res.-Atmos.*, **115**, D19121.
- Cecil, D. J., 2007: Satellite-derived rain rates in vertically sheared tropical cyclones. *Geophys. Res. Lett.*, **34**, L02811.
- Center, N. N. W. S. N. R. O., 1991. NOAA Next Generation Radar (NEXRAD) Level II Base Data. NOAA National Centers for Environmental Information. [Available online at <https://www.ncdc.noaa.gov/nexradinv/>.] Accessed 10 February 2016.
- Chen, S. Y. S., J. A. Knaff, and F. D. Marks, 2006: Effects of vertical wind shear and storm motion on tropical cyclone rainfall asymmetries deduced from TRMM. *Mon. Wea. Rev.*, **134**, 3190-3208.
- Corbosiero, K. L., and J. Molinari, 2003: The relationship between storm motion, vertical wind shear, and convective asymmetries in tropical cyclones. *J. Atmos. Sci.*, **60**, 366-376.
- Davis, C. A., S. C. Jones, and M. Riemer, 2008: Hurricane vortex dynamics during Atlantic extratropical transition. *J. Atmos. Sci.*, **65**, 714-736.
- DeMaria, M., M. Mainelli, L. K. Shay, J. A. Knaff, and J. Kaplan, 2005: Further improvements to the Statistical Hurricane Intensity Prediction Scheme (SHIPS). *Wea. Forecasting*, **20**, 531-543.
- Dvorak, V. F., 1975: Tropical cyclone intensity analysis and forecasting from satellite imagery. *Mon. Wea. Rev.*, **103**, 420-430.
- Harr, P. A., and R. L. Elsberry, 2000: Extratropical transition of tropical cyclones over the western North Pacific. Part I: Evolution of structural characteristics during the transition process. *Mon. Wea. Rev.*, **128**, 2613-2633.
- Hart, R. E., and J. L. Evans, 2001: A climatology of the extratropical transition of Atlantic tropical cyclones. *J. Climate*, **14**, 546-564.
- Hazelton, A. T., and R. E. Hart, 2013: Hurricane eyewall slope as determined from airborne radar reflectivity data: Composites and case studies. *Wea. Forecasting*, **28**, 368-386.
- Hill, K., and G. M. Lackmann, 2009: Influence of environmental humidity on tropical cyclone size. *Mon. Wea. Rev.*, **137**, 3294-3315.
- Huffman, G. J., and Coauthors, 2007: The TRMM multisatellite precipitation analysis (TMPA): Quasi-global, multiyear, combined-sensor precipitation estimates at fine scales. *Journal of Hydrometeorology*, **8**, 38-55.
- Jiang, H., C. Liu, and E. J. Zipser, 2011: A TRMM-based tropical cyclone cloud and precipitation feature database. *J. Appl. Meteorol. Climatol.*, **50**, 1255-1274.
- Jiao, L., Y. Liu, and H. Li, 2012: Characterizing land-use classes in remote sensing imagery by shape metrics. *ISPRS Journal of Photogrammetry and Remote Sensing*, **72**, 46-55.
- Jones, S. C., and Coauthors, 2003: The extratropical transition of tropical cyclones: Forecast challenges, current understanding, and future directions. *Wea. Forecasting*, **18**, 1052-1092.

- Jorgensen, D. P., 1984: Mesoscale and convective-scale characteristics of mature hurricanes. Part I: General observations by research aircraft. *J. Atmos. Sci.*, **41**, 1268-1285.
- Kain, J. S., 2004: The Kain-Fritsch convective parameterization: an update. *J. Appl. Meteor.*, **43**, 170-181.
- Kain, J. S., and J. M. Fritsch, 1990: A one-dimensional entraining/detraining plume model and its application in convective parameterization. *J. Atmos. Sci.*, **47**, 2784-2802.
- Kellner, O., D. Niyogi, M. Lei, and A. Kumar, 2012: The role of anomalous soil moisture on the inland reintensification of Tropical Storm Erin (2007). *Nat. Hazards*, **63**, 1573-1600.
- Klein, P. M., P. A. Harr, and R. L. Elsberry, 2000: Extratropical transition of western North Pacific tropical cyclones: An overview and conceptual model of the transformation stage. *Wea. Forecasting*, **15**, 373-395.
- Lawrence, M. B., L. A. Avila, J. L. Beven, J. L. Franklin, R. J. Pasch, and S. R. Stewart, 2005: Atlantic hurricane season of 2003. *Mon. Wea. Rev.*, **133**, 1744-1773.
- Li, Y., K. K. W. Cheung, and J. C. L. Chan, 2014: Modeling the effects of land-sea contrast on tropical cyclone precipitation under environmental vertical wind shear. *Quart. J. Roy Meteor. Soc.*, **141**, 396-412.
- Massam, B. H., and M. F. Goodchild, 1971: Temporal trends in the spatial organization of a service agency. *The Canadian Geographer/Le Géographe canadien*, **15**, 193-206.
- Matyas, C. J., 2007: Quantifying the shapes of US landfalling tropical cyclone rain shields. *The Professional Geographer*, **59**, 158-172.
- Matyas, C. J., 2008: Shape measures of rain shields as indicators of changing environmental conditions in a landfalling tropical storm. *Meteorological Applications*, **15**, 259-271.
- Matyas, C. J., 2009: A spatial analysis of radar reflectivity regions within Hurricane Charley (2004). *J. Appl. Meteorol. Climatol.*, **48**, 130-142.
- Matyas, C. J., 2010a: A geospatial analysis of convective rainfall regions within tropical cyclones after landfall. *International Journal of Applied Geospatial Research*, **1**, 69-89.
- Matyas, C. J., 2010b: Associations between the size of hurricane rain fields at landfall and their surrounding environments. *Meteorology and Atmospheric Physics*, **106**, 135-148.
- Matyas, C. J., 2014: Conditions associated with large rain-field areas for tropical cyclones landfalling over Florida. *Physical Geography*, **35**, 93-106.
- Matyas, C. J., 2017: Comparing the spatial patterns of rainfall and atmospheric moisture among tropical cyclones having a track similar to Hurricane Irene (2011). *Atmosphere*, **8**, 165-185.
- Matyas, C. J., S. E. Zick, and J. Tang, 2018: Using an object-based approach to quantify the spatial structure of reflectivity regions in Hurricane Isabel (2003): Part I: Comparisons between radar observations and model simulations. *Monthly Weather Review*, **146**, 1319-1340.
- National Oceanic and Atmospheric Administration, U. S. D. o. C.: Service Assessment: Hurricane Isabel, September 18-19, 2003. [Available online at <http://www.weather.gov/os/assessments/pdfs/isabel.pdf>.]
- Nolan, D. S., R. Atlas, K. T. Bhatia, and L. R. Bucci, 2013: Development and validation of a hurricane nature run using the joint OSSE nature run and the WRF model. *Journal of Advances in Modeling Earth Systems*, **5**, 382-405.
- Peng, M. S., R. N. Maue, C. A. Reynolds, and R. H. Langland, 2007: Hurricanes Ivan, Jeanne, Karl (2004) and mid-latitude trough interactions. *Meteorol. Atmos. Phys.*, **97**, 221-237.
- Rogers, R. F., S. S. Chen, J. Tenerelli, and H. E. Willoughby, 2003: A numerical study of the impact of vertical shear on the distribution of rainfall in Hurricane Bonnie (1998). *Mon. Wea. Rev.*, **131**, 1577-1599.

Shepherd, J. M., A. Grundstein, and T. L. Mote, 2007: Quantifying the contribution of tropical cyclones to extreme rainfall along the coastal southeastern United States. *Geophys. Res. Lett.*, **34**, L23810.

Skwira, G. D., J. L. Schroeder, and R. E. Peterson, 2005: Surface observations of landfalling hurricane rainbands. *Mon. Wea. Rev.*, **133**, 454-465.

Steiner, M., R. A. Houze, and S. E. Yuter, 1995: Climatological characterization of 3-dimensional storm structure from operational radar and rain-gauge data. *J. Appl. Meteor.*, **34**, 1978-2007.

Tiedtke, M., 1989: A comprehensive mass flux scheme for cumulus parameterization in large-scale models. *Mon. Wea. Rev.*, **117**, 1779-1800.

Velden, C., and Coauthors, 2006: The Dvorak tropical cyclone intensity estimation technique. *Bull. Amer. Meteor. Soc.*, **87**, 1195-1210.

Villarini, G., J. A. Smith, M. L. Baeck, T. Marchok, and G. A. Vecchi, 2011: Characterization of rainfall distribution and flooding associated with US landfalling tropical cyclones: Analyses of Hurricanes Frances, Ivan, and Jeanne (2004). *J. Geophys. Res.*, **116**, D23116.

Wang, W., and Coauthors, 2012: User's guide for Advanced Research WRF (ARW) modeling system version 3.

Xu, W., H. Jiang, and X. Kang, 2014: Rainfall asymmetries of tropical cyclones prior to, during, and after making landfall in South China and Southeast United States. *Atmos. Res.*, **139**, 18-26.

Zagrodnik, J. P., and H. Jiang, 2013: Investigation of PR and TMI version 6 and version 7 rainfall algorithms in landfalling tropical cyclones relative to the NEXRAD Stage-IV multi-sensor precipitation estimate dataset. *J. Appl. Meteorol. Climatol.*, **52**, 2809-2827.

Zhou, Y., and C. J. Matyas, 2018a: Spatial characteristics of rain fields associated with tropical cyclones landfalling over the western Gulf of Mexico and Caribbean Sea. *Journal of Applied Meteorology and Climatology*, **Under Review**

Zhou, Y., and C. J. Matyas, 2018b: Spatial characteristics of rain fields associated with tropical cyclones landfalling over the western Gulf of Mexico and Caribbean Sea. *Journal of Applied Meteorology and Climatology*, **Accepted May 15**

Zick, S. E., and C. J. Matyas, 2016: A shape metric methodology for studying the evolving geometries of synoptic-scale precipitation patterns in tropical cyclones. *Annals of the Association of American Geographers*, **106**, 1217-1235.